J Supercond Nov Magn (2015) 28:2517–2524
DOI 10.1007/s10948-015-3069-7

ORIGINAL PAPER

Magnetic and Structural Properties of Nanocrystalline Cobalt-Substituted Magnesium–Manganese Ferrite

Zein K. Heiba[1,3] · Mohamed Bakr Mohamed[2,3] · Adel Maher Wahba[4] · L. Arda[5]

Received: 9 March 2015 / Accepted: 3 April 2015 / Published online: 19 April 2015

Abstract A series of $Mg_{0.5}Mn_{0.5}Fe_{2-x}Co_xO_4$ ($0 \leq x \leq 0.5$) samples were synthesized by citrate precursor method. The impact of replacing Fe ions by Co on the structural parameters and magnetic properties of the system was investigated utilizing X-ray diffraction and M–H magnetic measurements at room and low temperatures. Phase analysis revealed a single-phase spinel for all samples, and cation distribution was suggested using data of magnetization loops, Rietveld analysis and then confirmed by Bertaut method. Both saturation magnetization and coercivity increase with Co content up to $x = 0.3$, then decrease slightly. The variation of lattice parameter, the interatomic distances, and the bond angles upon increasing the Co content was determined and then correlated with cation distribution and the magnetic behavior.

Keywords Nanostructures · Structure · Magnetic properties

✉ Mohamed Bakr Mohamed
mbm1977@yahoo.com

[1] Faculty of Science, Physics Department, Taif University, Al-Haweiah, Taif, Kingdom of Saudi Arabia

[2] Physics Department, Taibah University, Al-Madinah Al-Munawara, Kingdom of Saudi Arabia

[3] Faculty of Science, Physics Department, Ain Shams University, Cairo, Egypt

[4] Department of Engineering Physics and Mathematics, Faculty of Engineering, Tanta University, Tanta, Egypt

[5] Faculty of Arts and Sciences, Bahcesehir University, Ciragan Cad., Osmanpasa Mektebi Sok., No. 4, 34349, Besiktas, Istanbul, Turkey

1 Introduction

Spinel ferrites are highly versatile materials with applications in various technological fields; they are characterized by unique magnetic and electrical properties. Of these materials, the Mg–Mn ferrites have high initial permeability, high dc resistivity, low loss factor, high saturation magnetization with a rectangular hysteresis loop, high-frequency response, and relatively high Curie temperature, thereby quite beneficial for applications like memory and switching circuits, hyperthermia, resonance magnetic imaging and magnetic fluids [1–4]. For high frequency applications, the main desirable characteristics of ferrites are high dc resistivity, low dielectric losses, high initial permeability, and low saturation magnetization [5]. High initial permeability and high resistivity were obtained upon substituting In^{3+} in Mg–Mn ferrite [6]. Improvement in the dc resistivity has been observed at the expense of deterioration in the magnetic properties of Al^{3+} and Cr^{3+} substituted Mg–Mn ferrites [7].

Magnetic properties depend mainly on the cation distribution among the crystallographic sites available in the material lattice. On the other hand, the distribution of cations among the lattice sites depends on the procedure of material's preparations [8–10]. Spinel ferrites crystallize in the space group $Fd\bar{3}m$ with a unit cell containing 32 oxygen atoms. The unit cell contains 32 octahedral (16c and 16d) and 64 tetrahedral (8a, 8b, and 48f) sites. Among those available sites, only one eighth of the tetrahedral and half of the octahedral are occupied. Taking the center of symmetry at $\left(\frac{1}{4}\ \frac{1}{4}\ \frac{1}{4}\right)$, cations may occupy the tetrahedral site 8a at (000) (A site) and/or the octahedral site 16d at $\left(\frac{3}{8}\ \frac{3}{8}\ \frac{3}{8}\right)$ (B site). For $Mg_{0.5}Mn_{0.5}Fe_2O_4$ ferrite, Mg ions have a strong preference for occupying the octahedral B sites, while Mn ions prefer the tetrahedral A sites [11, 12]. Normally, Co ions prefer the B-site; nevertheless, partially

inverse Co ferrite was reported depending on the synthesis process [13].

In the present study, X-ray powder diffraction (XRD) with Rietveld analysis, transmission electron microscope (TEM), and magnetic measurements at room and low temperatures have been performed to find out the effect of Co doping in nanocrystalline $Mg_{0.5}Mn_{0.5}Fe_{2-x}Co_xO_4$, ($0 \leq x \leq 0.5$; step 0.1) on the microstructural parameters, cation distribution among the A and B sites, and the magnetic parameters of the system.

2 Experimental

$Mg_{0.5}Mn_{0.5}Fe_{2-x}Co_xO_4$ ($0 \leq x \leq 0.5$; step 0.1) samples were synthesized using stoichiometric amounts of iron, magnesium, and cobalt nitrates, manganese acetate, and citric acid using deionized water as a solvent. The solution was heated with stirring till the water evaporates. The gel was dried at 180 °C for 1 h, sintered at 400 °C for another hour, and then cooled to room temperature [14, 15]. X-ray diffraction patterns were collected using PANalytical diffractometer (X'pert MPD) with Cu-K_α radiation. The X-ray powder diffraction patterns of the samples were collected on a Philips diffractometer (X'pert MPD) with a goniometer using Cu-K_α radiation and a step-scan mode (step size $2\theta = 0.02°$; counting time 2 s) in the angular range 2θ = 10–80°. LaB_6 standard was used to correct instrumental broadening. The crystal structure and microstructure were refined by applying Rietveld profile method [16], using MAUD program [17]. The powder morphology was recorded using transmission electron microscope (TEM, JEOL JEM-100CX) with an accelerating voltage up to 100 kV. Magnetic measurements were carried out with the Quantum Design Model 6000 Vibrating Sample Magnetometer (VSM) option for the physical properties measurement system (PPMS) in magnetic field interval up to 4 T at 10 and 300 K.

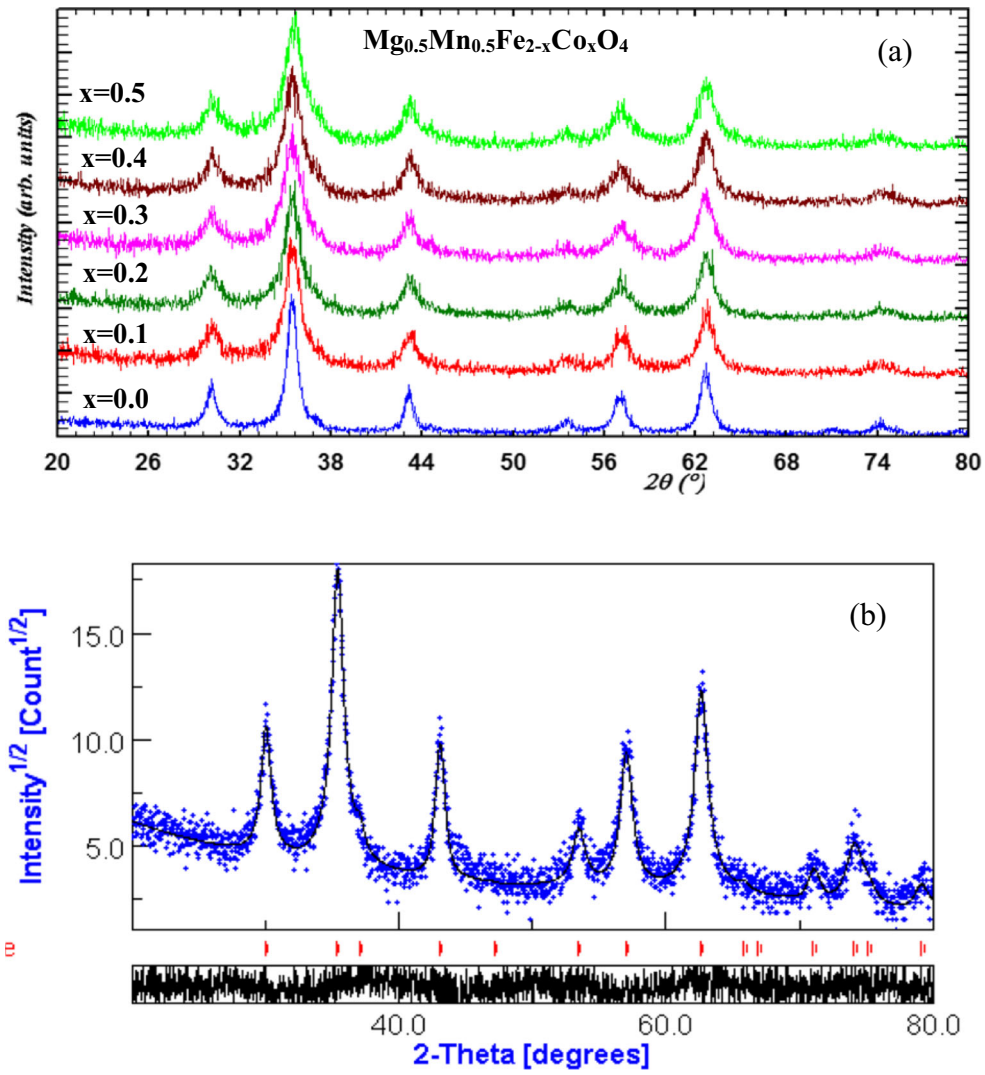

Fig. 1 **a** X-ray powder diffraction for $Mg_{0.5}Mn_{0.5}Fe_{2-x}Co_xO_4$ ($0 \leq x \leq 0.5$) and **b** Rietveld refinement profile for $Mg_{0.5}Mn_{0.5}Fe_2O_4$ sample

3 Results and Discussion

3.1 Structural and Microstructure Analysis

The X-ray diffraction patterns obtained for the prepared samples $Mg_{0.5}Mn_{0.5}Fe_{2-x}Co_xO_4$ ($0 \leq x \leq 0.5$) are shown in Fig. 1, where broad diffraction peaks indicate the nano nature of the prepared samples. Phase analysis revealed a single-phase spinel for all samples. The obtained diffraction patterns were used for structural and microstructural analysis applying Rietveld method; the obtained refined structural parameters are given in Table 1 and Fig. 2. X-ray is a poor tool in distinguishing between the atoms close to each other in the periodic table, e.g., Co and Fe. In Rietveld analysis, we used the cation distribution among the A and B sites obtained from magnetic analysis (in next section) as starting values for the refinement process. In order to confirm this suggested cation distribution for the single-phase samples, Bertaut method [18] was applied. Bertaut method relies on the choice of some of few reflections known to be sensitive to cation distributions, such as I_{220}/I_{400}, I_{220}/I_{422}, and I_{422}/I_{440}. The refinements of these chosen reflections were done, by minimizing the R factor defined as [18] follows:

$$R = \left| \left(\frac{I_{hkl}^{\text{Obs.}}}{I_{h\cdot k\cdot l\cdot}^{\text{Obs.}}} \right) - \left(\frac{I_{hkl}^{\text{Cal.}}}{I_{h\cdot k\cdot l\cdot}^{\text{Cal.}}} \right) \right|$$

All the observed intensities (I_{obs}) for the corresponding planes have to be corrected first by using Buerger formula [19]:

$$I_{hkl} = |F|_{hkl}^2 P L_{\text{p}},$$

where F is the structure factor, P is the multiplicity factor, and L_{p} is the Lorentz polarization factor for each (hkl) [20]. The displacement parameter corrections were neglected due to its small values. The best cations distribution obtained from Bertaut method were subjected to further refinements using Rietveld method and are shown in Table 1, the obtain cation distributions quite match with those obtain from magnetic measurements. Inspecting these cation distributions, one can notice the preference of Mg and Co to reside at the octahedral B site as expected [13, 21].

Figure 2 shows that upon replacing Fe^{3+} by Co^{2+}, the refined lattice parameter (a) firstly decreases for $x = 0.1$ and then increases continuously with increasing x. In addition, the crystallite size is reduced from 10.2 nm for $x = 0.0$ to 5.8 nm for $x = 0.1$, and then retain more or less the same value (≈5 nm) for the remaining samples. To achieve better view concerning the crystallite size and the morphology, the TEM image of $Mg_{0.5}Mn_{0.5}Fe_2O_4$ ferrite nanocrystals was obtained (Fig. 3). From the microstructure, it is clear that the nanoparticles are almost regular in shape and tend to agglomerate due to their mutual magnetic interactions. The matching between the crystallite size revealed from

Table 1 Refined values of oxygen positional parameter u, cation occupancies, and X-ray intensity ratio obtained from Rietveld refinements of $Mg_{0.5}Mn_{0.5}Fe_{2-x}Co_xO_4$

	x	0.0	0.1	0.2	0.3	0.4	0.5
	u	0.3670(13)	0.3724(14)	0.3729(14)	0.3734(14)	0.3745(18)	0.3695(14)
Cations occupancy factors							
A	Mg	0.110(9)	0.083(14)	0.169(15)	0.192(19)	0.195(19)	0.199(21)
	Mn	0. 490(9)	0.346(14)	0.336(15)	0.312(19)	0.280(19)	0.269(21)
	Co	0.0	0.012(14)	0.044(15)	0.074(19)	0.092(19)	0.119(21)
	Fe	0.389(9)	0.558(14)	0.452(15)	0.418(19)	0.435(19)	0.413(21)
B	Mg	0.195(9)	0.208 (16)	0.165(13)	0.153(17)	0.152(19)	0.151(21)
	Mn	0.005(9)	0.077(16)	0.081(13)	0.093(17)	0.110(19)	0.116(21)
	Co	0.0	0.044(16)	0.077(13)	0.114(17)	0.151(19)	0.190(21)
	Fe	0.806(7)	0.671(16)	0.672(13)	0.641(17)	0.581(19)	0.543(21)
X-ray intensity ratio ± 0.005							
I_{220}/I_{400}	Exp.	1.13	1.31	1.35	1.23	1.10	1.09
	Cal.	1.18	1.18	1.26	1.17	1.14	1.13
I_{400}/I_{440}	Exp.	0.78	0.81	0.65	0.87	0.73	0.79
	Cal.	0.63	0.70	0.67	0.64	0.69	0.63
I_{220}/I_{440}	Exp.	0.87	1.07	0.88	1.07	0.81	0.86
	Cal.	0.74	0.83	0.85	0.75	0.79	0.72

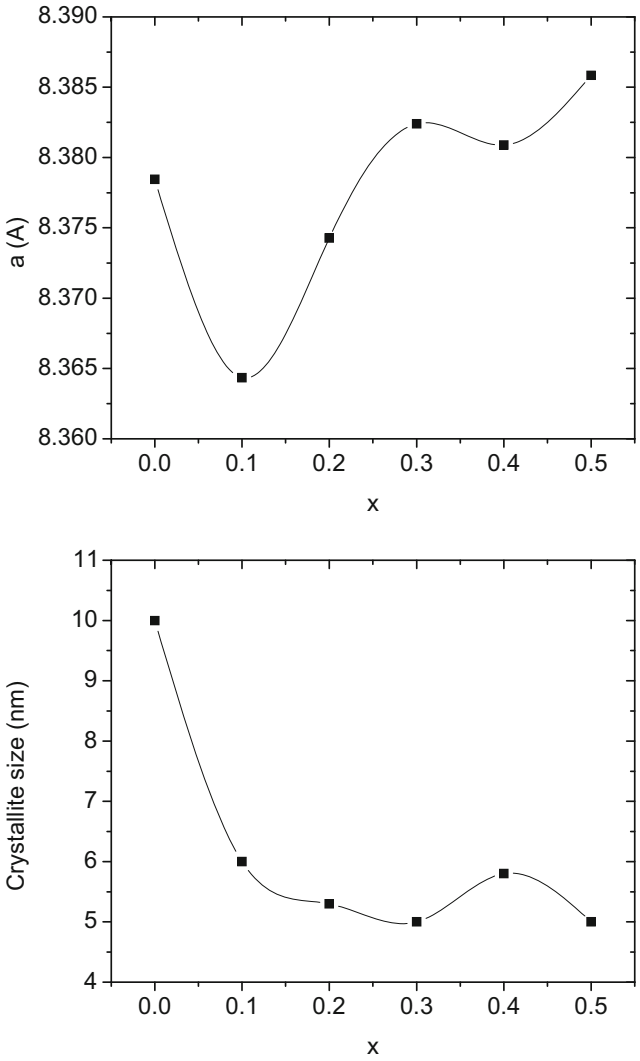

Fig. 2 Variation of lattice parameter, a, and crystallite size, D, with Co content x in $Mg_{0.5}Mn_{0.5}Fe_{2-x}Co_xO_4$ ($0 \leq x \leq 0.5$) system

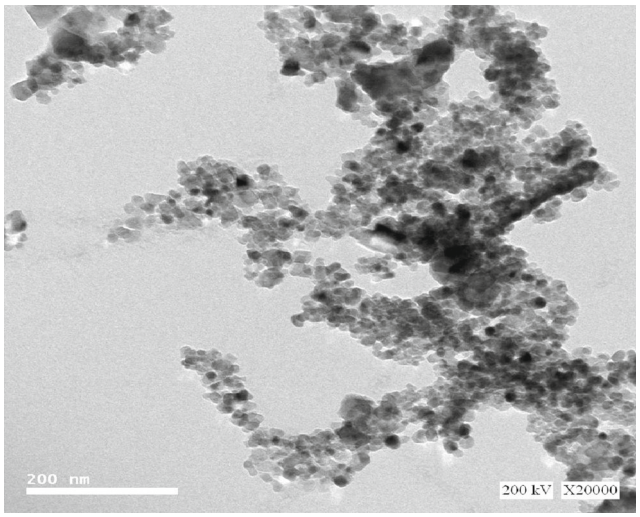

Fig. 3 TEM micrograph of the $Mg_{0.5}Mn_{0.5}Fe_2O_4$ sample

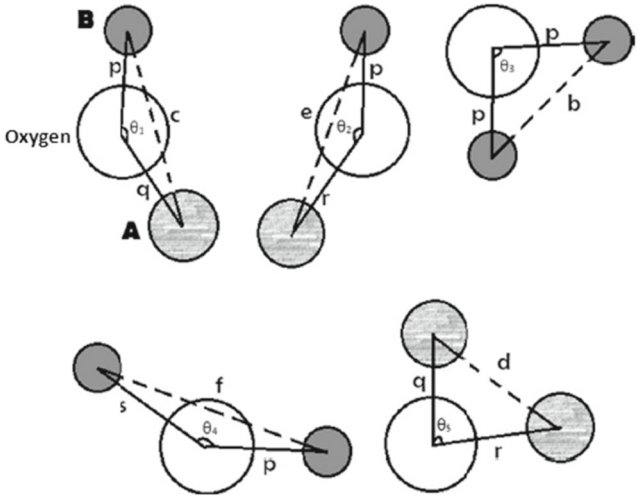

Fig. 4 Configuration of the ion pairs in spinel ferrites with favorable distances and angles

the TEM image and that obtained from Rietveld analysis is quite reasonable.

The ideal value of the positional parameter u is 0.375 for which the arrangement of O^{2-} ions is exactly a cubic closed packing. In actual spinel lattice, this ideal pattern is slightly deformed. For the present $Mg_{0.5}Mn_{0.5}Fe_{2-x}Co_xO_4$ system, $u < 0.375$ (see Table 1) indicating that O^{2-} ions move toward the cations in the tetrahedral A site along the ⟨111⟩ directions, which means that the tetrahedral interstices contract with a corresponding expansion of the octahedral B sites.

The bond lengths between cations (Me–Me) (b, c, d, e, and f), cations–anion (Me–O) (p, q, r, and s), and the bond angles (θ_1, θ_2, θ_3, θ_4, and θ_5) between the cations and cation–anion (Fig. 4) are given by following relations [22]:

$$p = a(5/8 - u) \qquad b = \sqrt{2}(a/4) \qquad \theta_1 = \cos^{-1}\left(\frac{p^2+q^2-c^2}{2pq}\right)$$
$$q = a\sqrt{3}(u - 1/4) \quad c = \sqrt{11}(a/8) \quad \theta_2 = \cos^{-1}\left(\frac{p^2+r^2-e^2}{2pr}\right)$$
$$r = a\sqrt{11}(u - 1/8) \; d = \sqrt{3}(a/4) \quad \theta_3 = \cos^{-1}\left(\frac{2p^2-b^2}{2p^2}\right)$$
$$s = a\sqrt{3}\left(\frac{u}{3} + 1/8\right) \; e = \sqrt{3}(3a/8) \quad \theta_4 = \cos^{-1}\left(\frac{p^2+s^2-f^2}{2ps}\right)$$
$$f = \sqrt{6}(a/4) \quad \theta_5 = \cos^{-1}\left(\frac{r^2+q^2-d^2}{2rq}\right)$$

The values of the interatomic distances between cation–anion (Me–O) and cation–cation (Me–Me) for $Mg_{0.5}Mn_{0.5}Fe_{2-x}Co_xO_4$ samples are listed in Table 2. Inspection of Table 2 reveals that the interatomic distances between the cation–anion (p, q, r, and s) and those between the cations (b, c, d, e, and f) change by increasing the Co concentration. This can lead to a change in the superexchange strength (wave function overlapping) with a resulting in the magnetic properties. Table 3 shows the estimated bond angles. From the results, the angles θ_1, θ_2, and θ_5 decrease, while θ_3 and

Table 2 Interatomic bond lengths between the cation–anion (p, q, r, and s) and between the cations (b, c, d, e, and f) for $Mg_{0.5}Mn_{0.5}Fe_{2-x}Co_xO_4$ samples

	Me–O (Å)				Me–Me (Å)				
x	p	q	r	s	b	c	d	e	f
0.0	2.1617	1.6979	3.3624	3.5893	2.9623	3.4736	3.6281	5.4421	5.1309
0.1	2.1147	1.7748	3.4347	3.6125	2.9599	3.4708	3.6251	5.4377	5.1267
0.2	2.1116	1.7830	3.4434	3.6168	2.9614	3.4726	3.627	5.4405	5.1294
0.3	21086	1.7913	3.4523	3.6213	2.9632	3.4746	3.6291	5.4437	5.1324
0.4	2.1006	1.8084	3.4697	3.6288	2.9649	3.4767	3.6312	5.4469	5.1354

θ_4 increase with higher Co^{2+} content. The angles θ_1, θ_2, and θ_5 suggest the weakening of the A–B and A–A interactions, while the decrease in θ_3 and θ_4 is indicative strengthening of the B–B interaction in the system. Generally, in ferrimagnetic materials, the increase in A–B (θ_1 and θ_2 angles) decreases the superexchange strength [22]. As Co^{2+} ions substitute iron in $Mg_{0.5}Mn_{0.5}Fe_{2-x}Co_xO_4$ matrix, the above situation are reverse; A–B (θ_1 and θ_2 angles) decrease; hence, superexchange strength is enhanced.

3.2 Magnetic Measurements

Magnetic characterization of the $Mg_{0.5}Mn_{0.5}Fe_{2-x}Co_xO_4$ samples was achieved through tracing room-temperature (RT) M–H curves (Fig. 5a) and hysteresis loops at 10 K (Fig. 5b), where both illustrate the variation of the magnetization as a function of the applied magnetic field extending up to 40 kOe. For both cases, the saturation point was not approached. This could be explained when considering the superparamagnetic nature of the produced samples. Hysteresis loops traced at 10 K were used to obtain the saturation magnetization (M_s) and the coercive field (H_c); values of M_s being deduced from the extrapolation of the M vs. $1/H$ curves to $1/H \rightarrow 0$ [23]. The variation of saturation magnetization and coercivity with Co^{2+} content is also illustrated in Fig. 6 where they showed similar trend, despite the inverse proportionality between H_c and M_s according to Brown's relation: $H_c = 2\ k_1/M_s$ [24], where k_1 is the magnetocrystalline anisotropy constant. This may be attributed to the dominating effect of increasing magnetocrystalline anisotropy with increasing Co^{2+} content.

Saturation magnetization of our samples is controlled mainly by the cation distribution of four elements with three of them being magnetic, namely Fe, Co, and Mn. In addition, the presence of more than one valence state for each of those three elements makes the matter more complicated. During the autocombustion process, oxidation of Mn^{2+} to Mn^{3+} [25–27] and Co^{2+} to Co^{3+} [28] is quite probable, while electron neutrality allows the subsequent presence of larger radius and less magnetic Fe^{2+} cation. The crystallite size for the whole samples is quite similar, and the combined effect of surface and local spin canting could be attributed to single canting angle for the magnetic moment of the B site, M_B. Spin canting effects highly explain the observed small M_s values of the present samples compared to the estimated ones. This behavior was reported for other ferrites and was interpreted in the light of core–surface model [29, 30] According to this model, the crystal grain can be divided into two parts, namely the core and the surface, with significantly different magnetic properties. For the grain surface, the spins possess highly random coordination, which frustrates the superexchange interaction, resulting in a canted spin configuration on the surface. Hence, it does not align completely in the direction of the applied magnetic field. For the core, it has a normal crystal structure, in which the single domain is formed. When the grain size equals the domain size, the observed magnetization originates mainly from the spin rotation of the core.

Table 3 Interatomic bond angles for $Mg_{0.5}Mn_{0.5}Fe_{2-x}Co_xO_4$ samples

x	θ_1	θ_2	θ_3	θ_4	θ_5
0	127.9	159.74	86.50	117.96	84.84
0.1	126.13	156.28	88.83	121.34	81.48
0.2	125.95	155.98	89.05	121.67	81.19
0.3	125.78	155.68	89.27	121.99	80.89
0.4	125.43	155.05	89.77	122.73	80.26

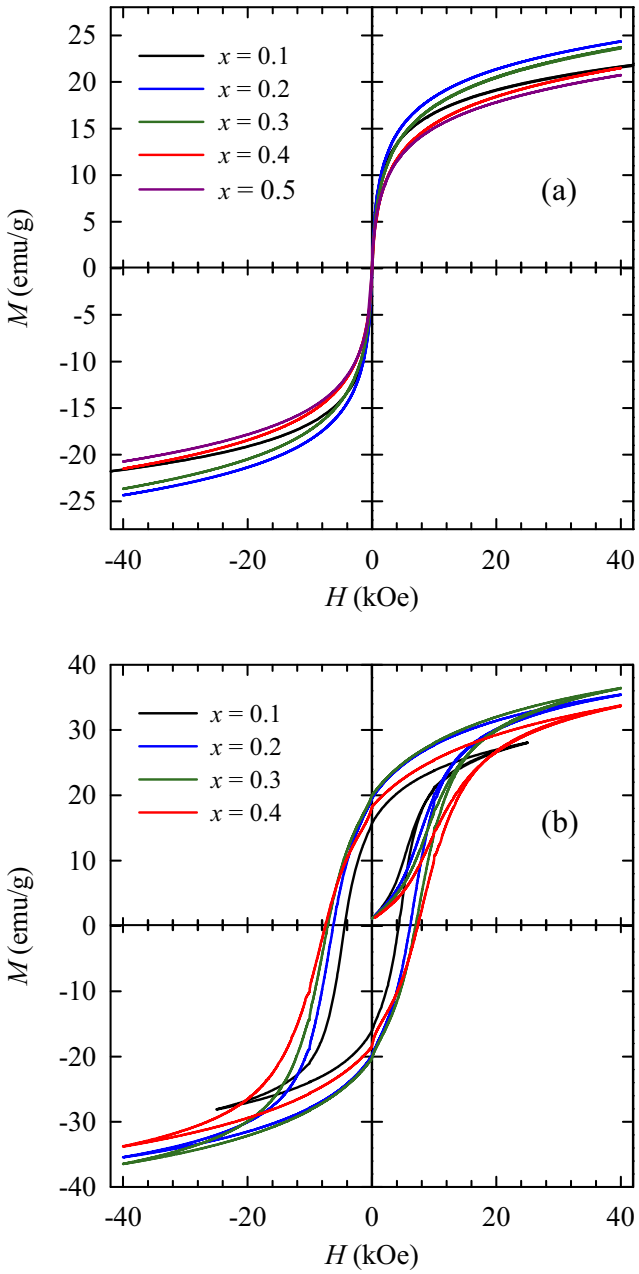

Fig. 5 **a** Room-temperature and **b** 10 K M–H curves for $Mg_{0.5}Mn_{0.5}Fe_{2-x}Co_xO_4$ ($0.1 \leq x \leq 0.5$) samples

The M_s data at 10 K were used to evaluate approximate values for the experimental magnetic moment per unit formula n_B^{obs} in units of the Bohr magneton μ_B, using the following formula [31]:

$$n_B^{\text{obs}} = \frac{\text{MW} \times M_s}{5585}$$

These values and the values of lattice parameters (a_{XRD}) were all used to suggest a cation distribution of the samples

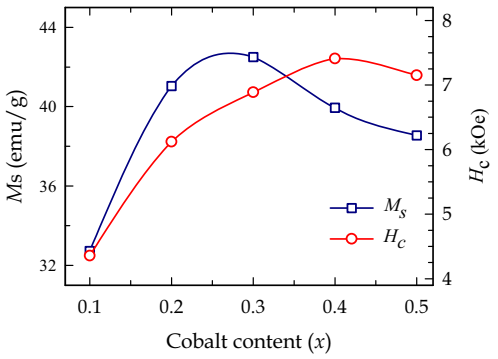

Fig. 6 Saturation magnetization (M_s) and coercive field (H_c) for $Mg_{0.5}Mn_{0.5}Fe_{2-x}Co_xO_4$ ($0.1 \leq x \leq 0.5$) samples at 10 K

of this work, as illustrated in Table 4. Values of n_B^{obs} are to be compared with the theoretical ones $n_{\text{Neel}} = M_B - M_A$ (obtained from the proposed cation distribution), where M_A and M_B are the A and B site sublattice magnetic moments, respectively. The values of the magnetic moments of the system constituent elements in terms of μ_B are 5, 4, 5, 4, 3, and 0 for Fe^{3+}, Fe^{2+}, Mn^{2+}, Mn^{3+}, Co^{2+}, and others, respectively. In fact, substituting the trivalent Fe ion with the divalent Co ion provides a significant source of nonstoichiometry of the prepared samples. However, the possibility of the oxidation of Mn^{2+} and/or Co^{2+} to Mn^{3+} and Co^{3+} reduces this effect. Comparison between the variation of both n_{Neel} and n_B^{obs} with Co^{2+} content is illustrated in Fig. 7, which shows a quite similar trend.

The increase of n_B^{obs} with $x \leq 0.3$ and its subsequent decrease for $x > 0.3$ could be explained as follows. Substituting Fe^{3+} with Co^{2+}, which has strong preference of occupying the B site, produces two competing effects. First, it displaces more nonmagnetic Mg^{2+} cations from the B site to A site and more magnetic Mn^{2+} from the A site to B site, and thus enhancing magnetization. On the other hand, substituting more Co^{2+} content increases nonstoichiometry and enhances the probability of producing the nonmagnetic Co^{3+} with the associated less magnetic $Mn^{3+}$and Fe^{2+} cations, all of which occupy the B site. Moreover, the small observed values of n_B^{obs} compared to those of n_{Neel} is attributed to the surface and local spin canting effects related to the small crystallite sizes of the present samples. The Yafet–Kittel [32] magnetic ordering of the local moments may further explain the small values of n_B^{obs}.

The saturation magnetization in Yafet–Kittle model is given by $M_s = M_B \cos\theta_{Y-K} - M_A$, where θ_{Y-K} is a Yafet–Kittel canting angle, which is estimated for our samples and are listed in Table 4, where their large values are attributed to the small crystallite sizes.

Table 4 Cation distribution of $Mg_{0.5}Mn_{0.5}Fe_{2-x}Co_xO_4$ ($0.1 \leq x \leq 0.5$) samples

x	Cation distribution	M_B (emu/g)	M_A (emu/g)	θ_{Y-K}(°)
0.1	$\left(Mg^{2+}_{0.084}Mn^{2+}_{0.346}Co^{2+}_{0.010}Fe^{3+}_{0.560}\right)\left[Mg^{2+}_{0.416}Mn^{2+}_{0.149}Mn^{3+}_{0.005}Co^{2+}_{0.085}Co^{3+}_{0.005}Fe^{2+}_{0.047}Fe^{3+}_{1.293}\right]O^{2-}_{3.932}$	7.673	4.560	39.25
0.2	$\left(Mg^{2+}_{0.169}Mn^{2+}_{0.330}Co^{2+}_{0.045}Fe^{3+}_{0.456}\right)\left[Mg^{2+}_{0.331}Mn^{2+}_{0.161}Mn^{3+}_{0.0009}Co^{2+}_{0.146}Co^{3+}_{0.009}Fe^{2+}_{0.027}Fe^{3+}_{1.317}\right]O^{2-}_{3.896}$	7.972	4.065	43.31
0.3	$\left(Mg^{2+}_{0.196}Mn^{2+}_{0.312}Co^{2+}_{0.072}Fe^{3+}_{0.420}\right)\left[Mg^{2+}_{0.304}Mn^{2+}_{0.169}Mn^{3+}_{0.019}Co^{2+}_{0.209}Co^{3+}_{0.019}Fe^{2+}_{0.019}Fe^{3+}_{1.261}\right]O^{2-}_{3.860}$	7.929	3.876	44.29
0.4	$\left(Mg^{2+}_{0.197}Mn^{2+}_{0.280}Co^{2+}_{0.090}Fe^{3+}_{0.433}\right)\left[Mg^{2+}_{0.303}Mn^{2+}_{0.170}Mn^{3+}_{0.050}Co^{2+}_{0.260}Co^{3+}_{0.050}Fe^{2+}_{0.012}Fe^{3+}_{1.155}\right]O^{2-}_{3.844}$	7.653	3.835	43.75
0.5	$\left(Mg^{2+}_{0.198}Mn^{2+}_{0.269}Co^{2+}_{0.118}Fe^{3+}_{0.415}\right)\left[Mg^{2+}_{0.302}Mn^{2+}_{0.166}Mn^{3+}_{0.065}Co^{2+}_{0.317}Co^{3+}_{0.065}Fe^{2+}_{0.001}Fe^{3+}_{1.084}\right]O^{2-}_{3.815}$	7.465	3.774	43.49

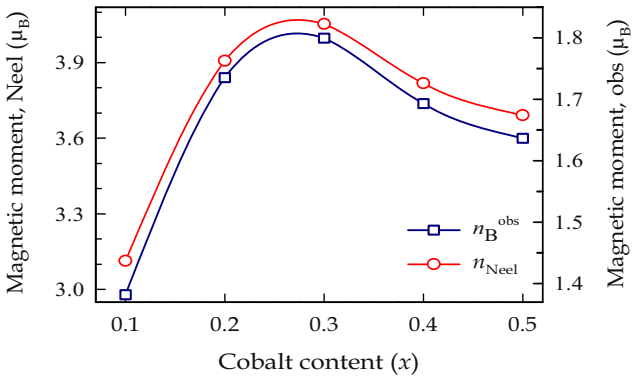

Fig. 7 Observed and theoretical magnetization moment for $Mg_{0.5}Mn_{0.5}Fe_{2-x}Co_xO_4$ ($0.1 \leq x \leq 0.5$) samples at 10 K

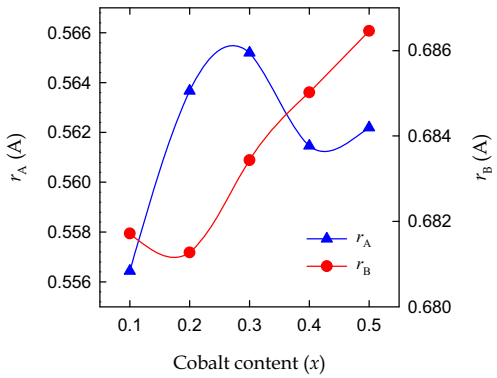

Fig. 8 Variation of the sublattice radii r_A and r_B with the cobalt content for $Mg_{0.5}Mn_{0.5}Fe_{2-x}Co_xO_4$ ($0.1 \leq x \leq 0.5$)

Further confirmation of the suggested cation distribution was obtained by applying a theoretical estimation of the lattice parameter for each composition and comparing it with that obtained by XRD analysis. For each sample, the average ionic radii per molecule of the tetrahedral and octahedral sites, r_A and r_B were calculated based on the suggested cation distribution of Table 4, using the following formulae [23]:

$$r_A = \sum_i \alpha_i r_i, \qquad r_B = \frac{1}{2}\sum_i \alpha_i r_i$$

where α_i is the concentration of the element i of ionic radius r_i on the respective side. The ionic radii for Mg^{2+} (0.57 and 0.72 Å), Mn^{2+} (0.66 and 0.83 Å), Fe^{3+} (0.49 and 0.645 Å), and Co^{2+} (0.58 and 0.745 Å) are taken with reference to both sites, with the first value corresponds to that of the A site. Both Mn^{3+} (0.645 Å), Co^{3+} (0.61 Å), and Fe^{2+} (0.78 Å) were assumed to occupy only the B site. Values of r_A and r_B are shown in Fig. 8, where the variation of r_A with Co content is quite similar to that of n_B^{obs}, which supports the suggested cation distribution. Theoretical values of the lattice parameter were then calculated from the following relation [23]:

$$a_{th} = \frac{8}{3\sqrt{3}}\left[(r_A + R_O) + \sqrt{3}\,(r_B + R_O)\right]$$

where R_O is the ionic radius of oxygen. The lattice parameters estimated from the suggested cation distribution match to less than 0.0001 % of that acquired from Rietveld analysis.

4 Conclusion

Single-phase nanocrystalline $Mg_{0.5}Mn_{0.5}Fe_{2-x}Co_xO_4$ ($0 \leq x \leq 0.5$) samples were synthesized by citrate precursor

method. Rietveld analysis revealed that the present system is neither normal nor inverse with a clear preference of Mg and Co to reside at the octahedral B site and Mn to reside at the A site as expected. The suggested cation distribution (obtained from Rietveld analysis then confirmed by Bertaut method and theoretical lattice parameter) accounts quite well for magnetization behavior and the variation of lattice parameter. The crystallite size decreases upon increasing Co content, while the refined lattice parameter (a) firstly decreases for $x = 0.1$ and then increases continuously for the higher values. Both saturation magnetization and coercivity increase with Co content up to $x = 0.3$ then decrease slightly. The bond angles θ_1, θ_2, and θ_5 decrease, while the angles θ_3 and θ_4 increase with introducing Co^{2+} in the matrix $Mg_{0.5}Mn_{0.5}Fe_{2-x}Co_xO_4$.

Compliance with Ethical Standards We declare that this is an original manuscript, and has *not* submitted to any other scientific journal inside the country or outside. In addition, we declare that this article has been written by us (the stated authors). We are aware of its content and approve its submission. We confirm that this manuscript (if accepted), will not be published in the same form, in any language, without the written consent of the publisher.

Conflict of interests There is no conflict of interest.

References

1. Iftikhar, A., Islam, M.U., Awan, M.S., Ahmad, M., Naseem, S., Iqbal, M.A.: J. Alloy. Comp. **601**, 116 (2014)
2. Jeyadevan, B., Chinnasamy, C.N., Shinoda, K., Tohji, K.: J. Appl. Phys **93**, 8450 (2003)
3. Azadmanjiri, J.: J. Non-Cryst. Solid **353**, 4170 (2007)
4. Gubbala, S., Nathani, H., Koizol, K., Misra, R.DK.: Physica B **348**, 317–328 (2004)
5. Bradley, F.N.: Materials for magnetic functions. Hayden Book Co. Inc., New York (1971)
6. Puri, B.K., Singh, M., Sud, S.P.: J. Mater. Sci. **29**, 2182–2186 (1994)
7. Singh, M., Sud, S.P.: Mater. Sci. Eng. **B83**, 180 (2001)
8. Heiba, Z.K., Hascicek, Y.S.: J. Appl. Cryst **38**(2), 306 (2005)
9. Heiba, Z.K., Arda, L., Bakr Mohamed, M., Al-Jalali, M.A., Dogan, N.: J. Supercond. Nov. Magn. **26**, 3299 (2013)
10. Heiba, Z.K., Bakr Mohamed, M., Fuess, H.: Cryst. Res. Technol. **47**, 535 (2012)
11. Kumar, G., Kanthwal, M., Chaulan, B.S., Singh, M.: Indian J. Pure Appl. Phys. **44**, 930 (2006)
12. Verma, S., Chand, J., Batoo, Kh.M., Singh, M.: J. Alloys Comp. **551**, 715 (2013)
13. Heiba, Z.K., Mostafa, N.Y., Abd-Elkader, O.H.: J. Magn. Magn. Mater. **368**, 246 (2014)
14. Heiba, Z.K., Mohamed Bakr Mohamed, M.A., Ahmed, M.A.A., Moussa, H.H., Hamdeh, J.: Alloy. Comp. **586**, 773 (2014)
15. Heiba, Z.K., Bakr Mohamed, M., Hamdeh, H.H., Ahmed, M.A.: J. Alloy. Comp. **618**, 755 (2015)
16. Lutterotti, L.: Maud 2.33, http://www.ing.unitn.it/~maud/
17. Rodriguez-Carvajal, J.: PhysicaB(Amsterdam) **192**, 55 (1993)
18. Weil, L., Bertaut, E.F., Bochirol, L.: J. Phys. Radium **11**, 208 (1950)
19. Buerger, M.J.: Crystal structure analysis. Wiley-Interscience, New York (1960)
20. Cullity, B.D.: The elements of X-ray diffraction. Addison Wesley), Reading (1956)
21. Ichiyanagi, Y., Kubota, M., Moritake, S., Kanazawa, Y., Yamada, T., Uehashi, T.: J. Magn. Magn. Mater. **310**, 2378–2380 (2007)
22. Karimi, Z., Mohammadifar, Y., Shokrollahi, H., KhamenehAsl, Sh., Yousefi, Gh., Karimi, L.: J. Magn. Magn. Mater. **361**, 150 (2014)
23. Maher Wahba, A., Bakr Mohamed, M.: Ceram. Int. **40**, 6127 (2014)
24. Bakr Mohamed, M., Yehia, M.: J. Alloy. Comp. **615**, 181 (2014)
25. Rath, C., Sahu, K.K., Anand, S., Date, S.K., Mishra, N.C., Das, R.P.: J. Magn. Magn. Mater. **202**, 77 (1999)
26. Thakur, A., Mathur, P., Singh, M.: J. Phys. Chem Solids **68**, 378 (2007)
27. Bakr Mohamed, M., Maher Wahba, A.: Ceram. Int. **40**, 11773 (2014)
28. Bakr Mohamed, M., Maher Wahba, A., Yehia, M.: Mater. Sci. Eng. B **90**, 52 (2014)
29. Li, J., Yuan, H., Li, G., Liu, Y., Leng, J.: J. Magn. Magn. Mater. **322**, 3396 (2010)
30. Bakr Mohamed, M., El-Sayed, K.: Mater. Res. Bull **48**(5), 1778 (2013)
31. Shaikh, P.A., Kambal, R.C., Rao, A.V., Kolekar, Y.D.: J. Alloys Compd. **492**, 590 (2010)
32. Alvarez, G., Montiel, H., Barron, J.F., Gutierrez, M.P., Zamorano, R.: J. Magn. Magn. Mater. **322**, 348 (2010)